Results in Engineering 20 (2023) 101631

Contents lists available at ScienceDirect

Results in Engineering

journal homepage: www.sciencedirect.com/journal/results-in-engineering

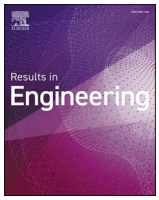

Effect of stress/strain partition on the mechanical behavior of heterostructured laminates: A strain gradient plasticity modeling

Xiaochong Lu [a], Jianfeng Zhao [b], Qi Wang [c], Hao Ran [a], Qingyuan Wang [a,d], Chongxiang Huang [a,*]

[a] School of Aeronautics and Astronautics, Sichuan University, Chengdu, 610065, China
[b] Institute of Systems Engineering, China Academy of Engineering Physics, Mianyang, Sichuan, 621999, China
[c] School of Electrical and Electronic Engineering, Nanyang Technological University, 50 Nanyang Avenue, 639798, Singapore
[d] Key Laboratory of Deep Earth Science and Engineering, Ministry of Education, Sichuan University, Chengdu, 610065, China

ARTICLE INFO

Keywords:
Heterostructured laminate
Strain and stress partition
Dispersed strain bands
Strain gradient plasticity
Finite element simulation

ABSTRACT

Based on the structure of natural nacres, laminated metal materials have been successfully developed to possess desirable mechanical properties for diverse engineering applications. These heterostructured (HS) laminates consist of layers with different mechanical performances, resulting in asynchronous deformation and intricate stress/strain partitioning behavior. These distinctive phenomena are crucial in achieving the strength-ductility synergy of HS laminates. Nonetheless, further investigations are imperative to gain a comprehensive understanding of local stress and strain evolutions during deformation, and to thoroughly explore the influence of stress/strain partition on the mechanical behavior of the HS laminates. This study utilized the conventional mechanism-based strain gradient (CMSG) plasticity theory to conduct finite element simulations. The tensile deformation of HS laminate comprising nanostructured (NS) bronze and coarse-grained (CG) copper layers was simulated as a benchmark. The simulation results revealed the following: (1) Stress partition and stress transfer between the layers occur during deformation and are influenced by the layer thickness; (2) Both strain partition and strain banding exist in the HS laminates with relatively thinner layers, and the formation of dispersed strain bands is related to the plastic strain gradient; (3) Heterogeneous deformation promotes strain delocalization and strain hardening, consequently leading to improved uniform elongation. This study provides valuable insights into the significant effect of stress/strain partition on the strength-ductility synergy of HS laminates from the perspective of constitutive modeling.

1. Introduction

The inhomogeneous microstructural architecture of heterostructured (HS) materials has effectively addressed the strength-ductility trade-off dilemma commonly observed in conventional metallic materials [1–6]. Thus, HS materials hold immense potential for use in critical engineering components. The presence of hetero-zones with starkly contrasting mechanical properties leads to synergistic effects [7,8]. As a result, HS materials exhibit superior strength-ductility synergy compared to their homogeneous counterparts, surpassing the predictions of the rule of mixture (ROM) [9,10]. As an ideal model material, HS laminates characterized by typical layer interfaces combine the advantages of different layers, such as high strength, significant strain hardening, substantial toughness, and considerable impact resistance [11–19]. More importantly, the fabrication of HS laminates can be achieved using conventional low-cost industrial techniques like accumulative roll bonding (ARB) [20–25], which support that the commercialization of HS laminates is more feasible than other advanced alloys. Therefore, the laminated design concept has been widely accepted to explore new metallic or non-metallic engineering materials with exceptional capabilities [26–30].

Hetero-deformation induced (HDI) stress plays a critical role in HS laminates, significantly contributing to strain hardening and strength-ductility synergy [22,31]. Hetero-zones in HS laminates can be categorized into hard layers (high strength, low ductility) and soft layers (low strength, high ductility). When these layers undergo loading, they experience distinct local deformation responses, leading to strain and stress partition [32]. Consequently, a strain gradient occurs at the layer

* Corresponding author.
E-mail address: chxhuang@scu.edu.cn (C. Huang).

https://doi.org/10.1016/j.rineng.2023.101631
Received 25 September 2023; Received in revised form 11 November 2023; Accepted 25 November 2023
Available online 30 November 2023

interface, generating geometrically necessary dislocations (GNDs) to ensure deformation continuity [33]. The accumulation of GNDs gives rise to long-range internal stresses [34,35], including back stress in soft layers and forward stress in hard layers. The interaction between the back and forward stresses leads to HDI stress [9,36], contributing to extra strain hardening. Furthermore, the piled-up GNDs act as barriers that hinder the movement of statistically stored dislocations (SSDs), thus also enhancing the strain hardening capacity of HS laminates [37].

It can be deduced that HDI stress can potentially modify the stress partition state during deformation. However, measuring stress distribution at the micro-scale poses significant challenges in experimental studies, leading to an incomplete understanding of the stress partitioning behavior and its effects. Furthermore, HS laminates displayed dispersed strain bands that span multiple layers, which can be considered an additional manifestation of strain partitioning behavior [14]. These strain bands effectively facilitate strain delocalization and enable the hard layer to accommodate substantial plastic strain [38]. An experimental study demonstrated the crucial role of microstructure inhomogeneity in triggering strain banding [39]. A theoretical investigation showed that stronger microstructure inhomogeneity leads to more stable strain bands [40]. While the strain gradient is known to drive strain banding in metallic glasses [41], the underlying formation mechanism of dispersed strain bands in HS laminates remains insufficiently explored [42]. As a result, it is imperative to employ reasonable constitutive modeling and simulations to further unravel the stress/-strain partitioning behavior of HS laminates.

Most existing constitutive models for HS materials have primarily focused on gradient [43–48] and bimodal [49,50] structures. Given the importance of strain gradient and GNDs in HS materials' deformation and strain hardening, strain gradient theories can provide valuable insights into the underlying deformation mechanisms and intrinsic factors [51]. The finite element method has been a reliable and widely used simulation approach to study the mechanical behavior of engineering materials and structures [52–54]. Up to now, several strain gradient models have been developed and implemented into the finite element method to simulate the deformation of HS materials [55–59]. For example, the mechanism-based strain gradient (MSG) plasticity theory based on the Taylor dislocation model has been utilized [60–63]. Such MSG theory involves high-order stresses and requires additional boundary conditions. High-order strain gradient theory can accurately describe the effects of multi-scale heterogeneity and high-order deformations at small length scales [64,65]. However, computational efficiency and convergence raise concerns due to the challenges of solving high-order stresses [66].

The conventional mechanism-based strain gradient (CMSG) plasticity theory, which is also based on the Taylor dislocation model, can capture the size effects at small scales without considering high-order stresses [67]. Therefore, CMSG theory offers higher calculating efficiency than high-order strain gradient theory, making it suitable for studying HS laminates. For instance, Wang et al. [68] utilized a CMSG finite element model to simulate the micropillar compression of Cu/Fe laminates. The results allowed for the analysis of stress and strain partition during deformation, as well as the evaluation of extra strain hardening promoted by GND accumulation. Similarly, Yuan and Du [69] employed CMSG theory and numerical analysis to investigate the influence of interfacial spacing on GND distribution and mechanical properties of HS laminates. Zhao et al. [70] developed a CMSG theory that accounted for the back stress resulting from internal heterogeneous deformation in Cu/Cu_{10}Zn laminates, and they successfully demonstrated the relationship between GND evolution and strain hardening. However, although these studies highlighted the ability of CMSG models to explain improvements in the mechanical properties of HS laminates, the stress/strain partitioning behavior was not thoroughly considered.

This paper aims to analyze the deformation mechanisms in HS laminates with varying layer thicknesses. The CMSG constitutive model was integrated into the finite element method to perform uniaxial tensile simulations. The paper is organized as follows: Section 2 elucidates the CMSG theory and simulation methodologies; Section 3 analyzes the stress/strain partitioning behavior, the effect of heterogeneous deformation, and the extra strain hardening in HS laminates based on the simulation results; Section 4 concludes the findings of this investigation.

2. Methodology

In this section, the employed CMSG plasticity theory is described, along with a brief introduction to the experimental background used for the simulations. Details regarding the finite element models are provided, which were constructed based on experimental measurements, including information on geometric dimensions, meshes, and boundary conditions. Furthermore, the calibrated parameters and simulation results for homostructured copper and bronze are presented.

2.1. Conventional mechanism-based strain gradient (CMSG) formulation

In the CMSG theory, high-order terms are not involved, the calculations of strain and stress are the same as those in classical plasticity theory, and the plastic strain gradient is obtained from the plastic strain increment. Therefore, only the constitutive model of the CMSG theory incorporates the plastic strain gradient, while the equilibrium equations and boundary conditions remain the same as those in conventional continuum theories [67]. The plastic strain rate is calculated using a visco-plastic formulation [67]

$$\dot{\varepsilon}^{\mathrm{p}} = \dot{\varepsilon}\left[\frac{\sigma_{\mathrm{eff}}}{\sigma_{\mathrm{flow}}}\right]^{m}, \tag{1}$$

where $\dot{\varepsilon}$ is the strain rate, $\sigma_{\mathrm{eff}} = \sqrt{\frac{3}{2}\sigma_{ij}^{'}\sigma_{ij}^{'}}$ is the effective stress, σ_{flow} is the flow stress, and m is the rate-sensitivity exponent. According to the Taylor dislocation model, the flow stress is calculated based on the current dislocation density [71]

$$\sigma_{\mathrm{flow}} = M\alpha Gb\sqrt{\rho_{\mathrm{SSD}} + \rho_{\mathrm{GND}}}, \tag{2}$$

where M is the Taylor factor, α is the empirical coefficient, G is the shear modulus, b is the magnitude of the Burgers vector, ρ_{SSD} and ρ_{GND} are the densities of GNDs and SSDs, respectively. GND density is directly related to the plastic strain gradient, which is expressed by [72,73]

$$\rho_{\mathrm{GND}} = \bar{r}\frac{\eta^{\mathrm{p}}}{b}, \tag{3}$$

where $\bar{r}$= 1.9 is the Nye factor for face-centered cubic (FCC) polycrystals [72,74], $\eta^{\mathrm{p}} = \sqrt{\frac{1}{4}\eta_{ijk}^{\mathrm{p}}\eta_{ijk}^{\mathrm{p}}}$ is the effective plastic strain gradient [60]. For the uniform deformation cases, the values of η^{p} and ρ_{GND} are zero. The SSD density can be expressed with the consideration of $\sigma_{\mathrm{flow}} = \sigma_{\mathrm{ref}}f(\varepsilon^{\mathrm{p}})$.

$$\rho_{\mathrm{SSD}} = \left[\frac{\sigma_{\mathrm{ref}}f(\varepsilon^{\mathrm{p}})}{M\alpha Gb}\right]^{2}. \tag{4}$$

Substituting Eqs. (3) and (4) into Eq. (2) gives the flow stress under inhomogeneous plastic deformation

$$\sigma_{\mathrm{flow}} = M\alpha Gb\sqrt{\left[\frac{\sigma_{\mathrm{ref}}f(\varepsilon^{\mathrm{p}})}{M\alpha Gb}\right]^{2} + \bar{r}\frac{\eta^{\mathrm{p}}}{b}} = \sigma_{\mathrm{ref}}\sqrt{f^{2}(\varepsilon^{\mathrm{p}}) + l\eta^{\mathrm{p}}}, \tag{5}$$

where l is the intrinsic material length parameter, $\sigma_{\mathrm{ref}} = \sigma_{\mathrm{y}}(E/\sigma_{\mathrm{y}})^{n}$ is the reference stress, $f(\varepsilon^{\mathrm{p}}) = (\varepsilon^{\mathrm{p}} + \sigma_{\mathrm{y}}/E)^{n}$ is the non-dimensional function of the plastic strain (σ_{y} is the yield stress, E is the elastic modulus, and n is the strain hardening exponent). It is worth noting that the layer thickness dependence of the HS laminates' yield stress could not be accurately captured by the CMSG theory [70]. Thus, a modified model describing the yield stresses of HS laminates with different layer thicknesses is employed in this study [75]

$$\sigma_y = \sigma_0 + kh^{-1/2}, \quad (6)$$

where k is the slope, h is the layer thickness, and σ_0 is the lattice friction stress [75].

The CMSG model described above was implemented into the finite element software Abaqus through the user-define material subroutine (UMAT). An essential part of the UMAT implementation is evaluating the plastic strain gradient η^p. The calculating process of the effective plastic strain gradient is elaborated in Appendix A. More details on the numerical implementation can be found in the literature [74].

2.2. Experimental background

The experimental data utilized in this study for modeling and parameter calibration was obtained from the authors' previous investigation [14]. Here, a concise overview of the preparation, uniaxial tensile test, and microstructures of the specimens is provided. The HS laminates were fabricated using commercial copper (99.9 %) and bronze (Cu-10 wt%Zn) sheets through the ARB technique. The layer thicknesses of the specimens were controlled by cold rolling as 125, 62, 31, 15, 7.5, and 3.7 μm. Subsequently, all laminated samples were subjected to annealing at 220 °C for 2 h, leading to the recrystallization in copper layers but not in bronze layers. Therefore, the coarse-grained (CG) copper layer has equiaxed grains with an average size of 4.8 μm and random orientations. In contrast, the nanostructured (NS) bronze layer exhibited nano-scale lamellar grains with an average size of 100 nm.

The tensile specimen was designed in a dog-bone shape with a gauge length of 12 mm and a width of 2 mm. The loading strain rate was set to 5×10^{-4} s^{-1}, and an extensometer was used to measure the strain. Moreover, an *in-situ* tensile test was conducted within a scanning electron microscope (SEM). Digital image correlation (DIC) characterization was performed initially at an engineering strain of 0.2 % and subsequently at a strain interval of 1.1 % until sample failure occurred. The gauge section of the specimen had a defined area of 6.0×0.5 mm^2. Random speckle patterns were prepared on the gauge section to ensure high-resolution quality, achieving a spatial resolution of 171 nm/pixel.

2.3. Finite element models and boundary conditions

Two-dimension finite element models were established for the HS laminates and discretized into 12,800 CPE8R elements with reduced integration, as shown in Fig. 1(a). All models consist of eight layers; however, their different layer thicknesses result in varying widths and heights, as specified in Table 1. Appropriate boundary conditions were applied to simulate the uniaxial tensile deformation, as depicted in Fig. 1 (b). Initially, periodic boundary conditions along the Y-axis were applied at the upper and bottom boundaries using the Abaqus plugin EasyPBC [76]. Subsequently, a displacement load corresponding to an engineering strain of 15 % was applied along the X-axis at a reference point, coupled with the other nodes on the right boundary. The loading strain rate was set to match the experimental conditions [14], and the loading displacements for each model are also given in Table 1. Additionally, all the nodes on the left boundary were constrained along the X-axis to prevent rigid body movements, as well as the bottom node of the left boundary along the Y-axis. Finally, the displacement and reaction force along the X-axis at the reference point were extracted to calculate the engineering strain ε_{eng} and engineering stress σ_{eng}, respectively. The true strain-stress curves were derived from the engineering strain-stress curves using $\varepsilon_{true} = \ln(1+\varepsilon_{eng})$ and $\sigma_{true} = \sigma_{eng}(1+\varepsilon_{eng})$.

2.4. Parameter calibration

The constitutive parameters used in the finite element simulations are listed in Table 2. The elastic modulus E and Poisson's ratios ν of the NS bronze and CG copper were adopted from the literature [69], as well as the strain hardening exponent n of CG copper [74]. For FCC polycrystals, the commonly used Taylor factor M is 3.06 [77–79]. The empirical coefficient α typically falls in the range of 0.3–0.5 [68], and $\alpha = 0.5$ is utilized in this study. The yield stress σ_y is obtained from the experimental measurements [14]. The material length scale l and the strain hardening exponent n of NS bronze were calibrated by fitting the tensile strain-stress curves of CG copper and NS bronze [14]. For homogeneous materials, the second term of Eq. (6) $kh^{-1/2}$ is irrelevant. The finite element models of CG copper and NS bronze have the same

Table 1
Geometric dimensions of the finite element models (unit: μm).

Label	Layer thickness	Width	Height	Displacement
Laminate-125	125	800	1000	120
Laminate-62	62	396.8	496	59.52
Laminate-31	31	198.4	248	29.76
Laminate-15	15	96	120	14.4
Laminate-7.5	7.5	48	60	7.2
Laminate-3.7	3.7	23.68	29.6	3.552

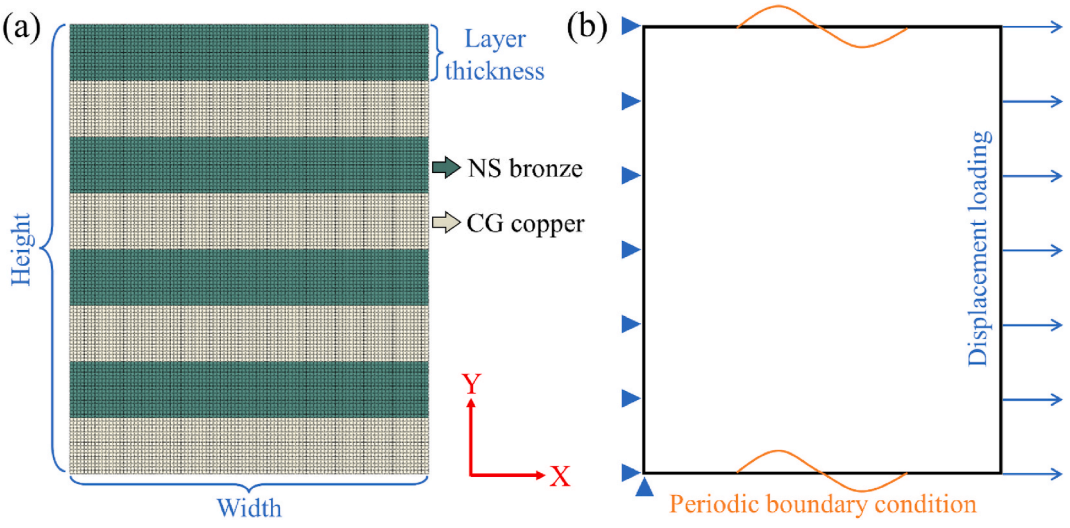

Fig. 1. The eight-layer finite element model established for the HS laminate and the boundary conditions:(a) Two-dimension finite element model of the HS laminate with 12,800 CPE8R elements; (b) Boundary conditions applied to the finite element model to simulate the uniaxial tensile deformation.

Table 2
Constitutive parameters for CG copper and NS bronze.

Symbol	Description (unit)	CG copper	NS bronze
E	Elastic modulus (MPa)	115,000	115,000
ν	Poisson's ratio	0.324	0.307
M	Taylor factor	3.06	3.06
α	Empirical coefficient	0.5	0.5
σ_y	Yield stress (MPa)	62	430
l	Material length scale (μm)	0.5	0.5
n	Strain hardening exponent	0.2	0.07

dimension of 800 × 1000 μm^2 with 12,800 CPE8R elements. The true strain-stress curves of CG copper and NS bronze are obtained through uniaxial tensile simulations, as presented in Fig. 2. It is evident that the simulation results exhibit good agreement with the experimental data, affirming the validation of simulation methodologies and constitutive parameters.

3. Results and discussion

This section presents the results of uniaxial tensile simulation conducted on CG copper/NS bronze laminates with varying layer thicknesses. The simulation results include the strain-stress curves and the evolutions of dislocation densities. By analyzing both the internal variables of the constitutive model and the field variables of the finite element method, this study investigates the strain/stress partition, strain banding, and their correlation with the strain gradient. Furthermore, the role of heterogeneous deformation in the strength-ductility synergy of the HS laminates is discussed.

3.1. Overall strain-stress response

Based on the methodology outlined in Section 2, uniaxial tensile deformations were simulated for the HS laminates with six different layer thicknesses. However, it is important to note that the value of σ_y (yield stress) in Table 2 needs to be adjusted due to the strengthening caused by decreasing interfacial spacing in the HS laminates. Consequently, the yield stress should be determined according to Eq. (6). Subsequently, the evolution of experimental yield stress with decreasing layer thickness was fitted, as illustrated in Fig. 3(a), and the slope was determined to be $k = 3.95$ MPa·mm$^{-1/2}$. However, the intercept of 263.2 MPa is suitable for the whole HS laminate but could not serve as the parameter for the individual CG copper or NS bronze layers. Therefore, the lattice friction stresses σ_0 for CG copper and NS bronze are set to 32 MPa and 400 MPa, respectively (30 MPa lower than the values in Table 2), to achieve improved fitting accuracy. In addition, the remaining parameters were kept consistent with those in Table 2. The simulated true strain-stress curves and the experimental data are presented in Fig. 3(b). The comparison demonstrates that the CMSG plastic model effectively captures the deformation behaviors of CG copper/NS bronze laminates with different layer thicknesses, including yielding and strain hardening.

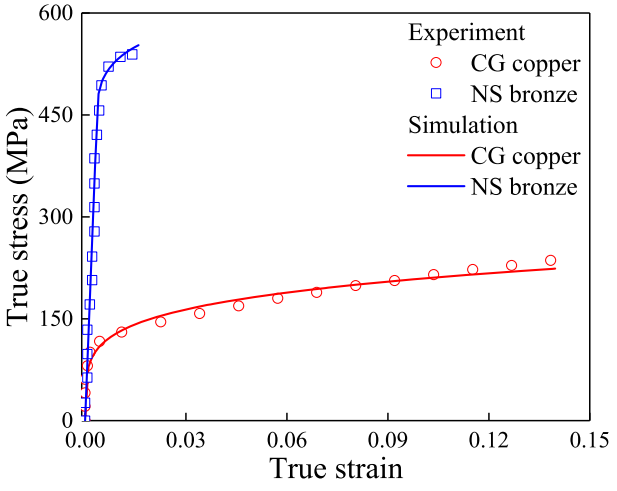

Fig. 2. Comparisons between the experimental and simulated strain-stress curves of the CG copper and NS bronze during uniaxial tensile deformation.

Moreover, Fig. 3(c-d) show the evolutions of GND and SSD densities with respect to the equivalent plastic strain. It can be observed that there is almost negligible GND accumulation in the HS laminates with layer thicknesses ranging from 15 to 125 μm, indicating a weak strain gradient effect during deformation. However, as the layer thickness decreases, the improvement in GND density becomes more significant, particularly in Laminate-3.7. Therefore, although all the NS bronze/CG copper laminates have the same layer thickness ratio, the strain gradient effect is only activated when the layer thickness approaches the intrinsic length scale. Furthermore, Fig. 3(d) gives the evolution of SSD density. The increasing rate of SSD density becomes more pronounced as the layer thickness decreases. According to Eq. (2), the accumulations of both GNDs and SSDs lead to an increase in flow stress and contribute to strain hardening [80]. In addition, comparing Fig. 3(c) and (d), the GND density approaches the SSD density in Laminate-3.7 at a large strain, suggesting that GNDs and SSDs contribute similarly to strain hardening in the HS laminate with thinner layers. Interestingly, the maximum equivalent plastic strain exceeds the maximum true strain, indicating non-uniform deformation and a multiaxial stress state within the HS laminates [81].

3.2. Stress partition and stress transfer

The stress distributions within the CG copper/NS bronze laminates were further analyzed based on the simulation results. Fig. 4(a) shows the stress component σ_{11} along the loading direction (X-axis) for each layer at an engineering strain of 15 %. Remarkable stress partition is observed due to the different mechanical properties of NS bronze (hard zone) and CG copper (soft zone) layers. Specifically, the hard zones experience higher stress levels than the soft zones. Moreover, both zones exhibit improved stresses as the layer thickness decreases. The stress partitioning behavior results in different contributions from NS bronze and CG copper layers to the overall flow stress. Fig. 4(b) presents that the stress difference between the hard and soft zones becomes more pronounced with increasing layer thickness.

The proportion of stress contributed by NS bronze layers to the overall flow stress is calculated by $R_B = \sigma_B/(\sigma_B + \sigma_C)$, while that of the CG copper layer is $R_C = 1 - R_B$. This analysis is further visualized in Fig. 4(c), which depicts the stress contributions from the NS bronze and CG copper layers, reflecting the evident stress partition and transfer during deformation. The whole deformation process can be divided into two stages. At *Stage A*, the contribution of the hard zones quickly increases and reaches a maximum, accompanied by a decrease in the contribution of the soft zones. However, at *Stage B*, occurring after a true strain of 0.4 %, the trends are reversed: the contribution of the CG copper layer gradually increases, while that of the NS bronze layer decreases. This phenomenon can be attributed to the stress transfer from the hard zone to the soft zone, which results from the relatively better strain hardening ability of the CG copper layers. Notably, the total change in stress percent of the hard or soft zones during *Stage B* becomes less obvious as the layer thickness increases, as shown in Fig. 4(d).

3.3. Strain partition and strain banding

Fig. 5(a-b) compare the logarithmic strain (LE) contours for Laminate-125 and Laminate-3.7 at an engineering strain of 15 %. The results reveal a noticeable strain partition, with the CG copper layer bearing more deformation than the NS bronze layer. However, for Laminate-3.7 with a smaller layer thickness, dense dispersed strain

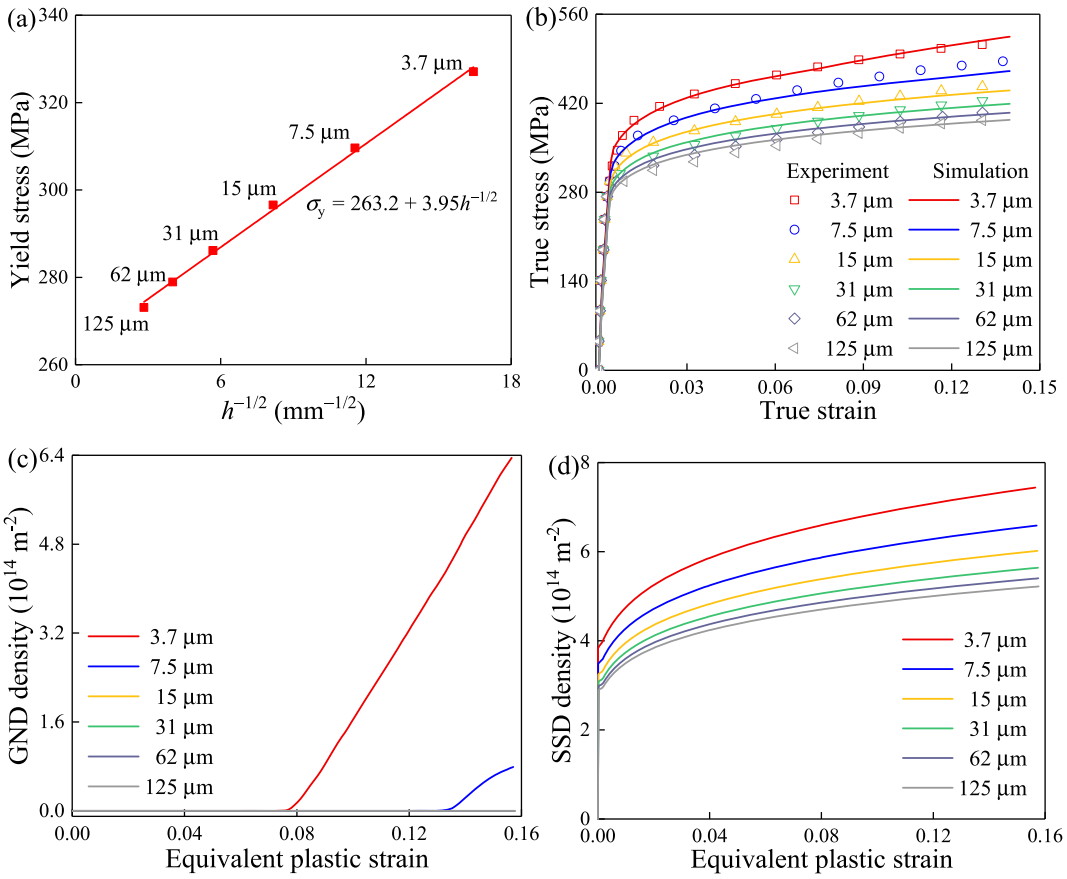

Fig. 3. Fitting process of the slope k in Eq. (6) and the simulation results of HS laminates with different layer thicknesses. (a) Experimental yield stress versus the $-1/2$ power of layer thickness, the slope k is obtained by fitting the distribution curve; (b) Comparisons between the experimental and simulated true strain-stress curves; (c) GND density and (d) SSD density evolutions in different HS laminates with increasing equivalent plastic strain.

bands can be observed, as depicted in Fig. 5(b). These strain bands traverse different layers and are oriented approximately 45° from the loading direction, indicating the presence of coupled deformation between the NS bronze and CG copper layers. It is important to note that strain bands were also observed in experiments using the high-resolution micro-DIC technique [14], as shown in Fig. 5(c). Encouragingly, the simulated strain contours in Fig. 5(b) exhibit strikingly similar to the experimental measurements, reflecting the reliability of the simulation methods employed in this study.

Fig. 6 illustrates the contours of equivalent plastic strain for Laminate-3.7 under various engineering strains. When the engineering strain is below 5 %, only strain partition occurs, and both the plastic strains in the CG copper and NS bronze layers improve with increasing deformation. At an applied strain of 10 %, strain banding becomes apparent in both the NS bronze and CG copper layers. The strain bands exhibit a relatively concentrated distribution, as evidenced by Fig. 6(c). When the applied strain reaches 15 %, the strain bands become more diffuse, and the magnitudes of plastic strain in different layers become more similar. Furthermore, Fig. 6(d) demonstrates the coexistence of strain partition and strain banding, suggesting a synergistic relationship between these two deformation mechanisms rather than mutual inhibition.

Similar dispersed strain bands have also been observed in other HS metallic materials during tensile deformation, such as gradient and lamella structures [82,83]. These strain bands are crucial in promoting strain delocalization and facilitating deformation coupling between different layers, thereby serving as a unique deformation mechanism in HS materials [82]. However, the specific mechanism underlying the formation of such dense strain banding remains inadequately understood, necessitating further investigations [9]. The following section analyzes the distributions and evolutions of strain, strain gradient, and GND density based on simulation results to identify potential mechanisms responsible for strain banding in HS laminates.

3.4. Mechanism of strain band formation

Fig. 5(a-b) reveal that strain banding is more likely to be activated in the HS laminate with a thinner thickness, i.e., smaller interfacial spacing. Wu et al. [84] proposed that strain bands arise due to the constraint imposed by incompatible deformation between adjacent layers. As the deformation progresses, the stress state in each layer changes from uniaxial to multiaxial, promoting the activation of additional dislocation slip systems. However, this explanation does not account for the influence of layer thickness on the initiation of strain banding. Fig. 3(c) demonstrates that Laminate-3.7 has a significantly higher GND density than Laminate-125, indicating a strong strain gradient effect in Laminate-3.7. Hence, it is reasonably hypothesized that the formation of strain bands is linked to the plastic strain gradient.

To further substantiate this assertion, the contours of logarithmic strain ε_{LE}, effective plastic strain gradient η^p, and GND density ρ_{GND} at applied engineering strains of 7.2 %, 10 %, and 15 % are shown in Fig. 7. It is noteworthy that the distribution of ρ_{GND} exhibits excellent conformity with η^p contour. Regions with high η^p correspond to areas where ε_{LE} undergoes significant variations. At an applied strain of 7.2 %, the occurrence of newly formed strain bands is sporadic and localized. With increasing deformation, the pre-existing strain bands become more dispersed, while additional strain bands emerge in other regions. Moreover, the areas with significant plastic strain gradients also expand. From Fig. 7, the nucleation mechanism of strain bands was understood, which can be elucidated as follows.

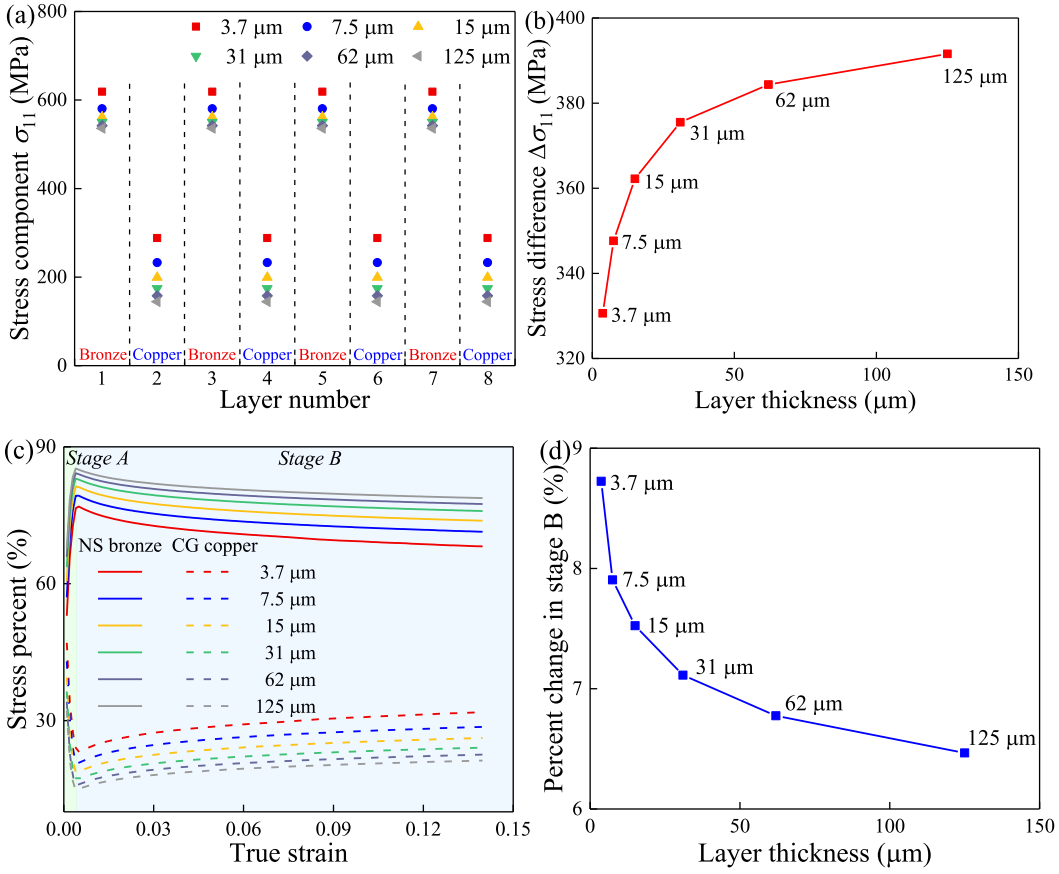

Fig. 4. Stress partition in the HS laminates with different layer thicknesses: (a) Stress component along the X-axis (loading direction) of each layer at the final deformation frame with an engineering strain of 15 %; (b) Stress difference between the NS bronze and CG copper layers; (c) Contribution evolutions of the NS bronze and CG copper layers to the flow stress with increasing true strain; (d) Change in stress percent of NS bronze or CG copper layer during *Stage B*.

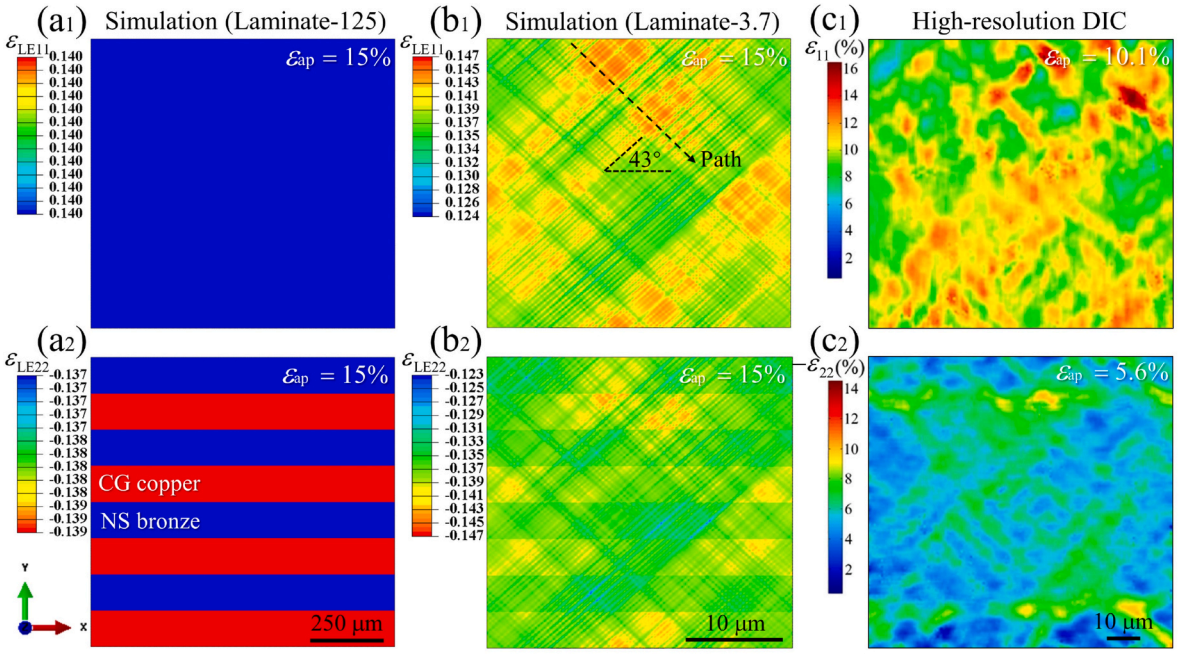

Fig. 5. Comparison between the simulated strain contours and the micro-DIC measurement in experiments. The logarithmic strain (LE) components along the X-axis (LE11) and Y-axis (LE22) at an applied engineering strain of 15 % in (a) Laminate-125 and (b) Laminate-3.7; (c) Experimental measurement of the strain distribution in the NS bronze/CG copper laminate by high-resolution micro-DIC technique [14].

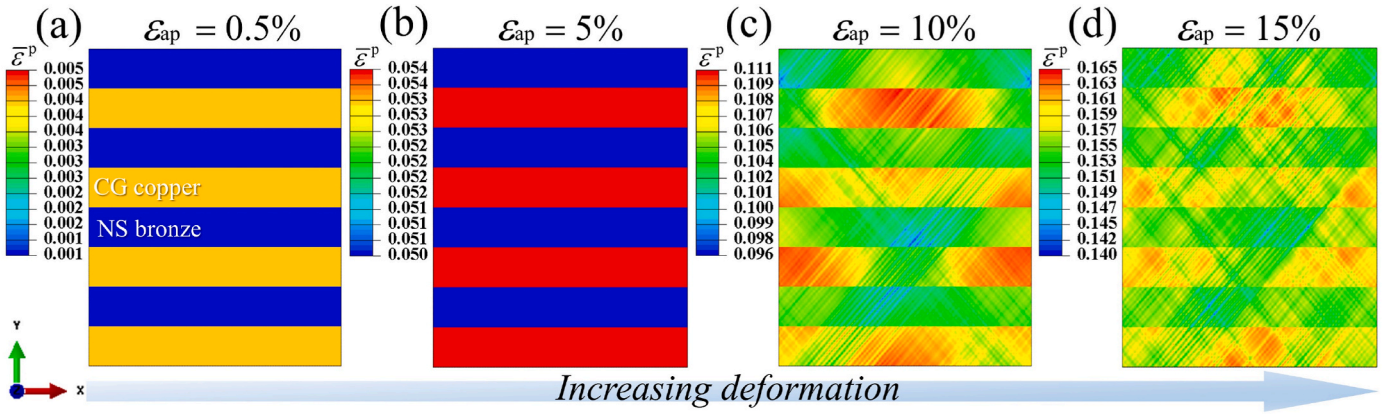

Fig. 6. Simulated equivalent plastic strain contours of Laminate-3.7. The corresponding applied engineering strains are (a) 0.5 %, (b) 5 %, (c) 10 %, and (d)15 %.

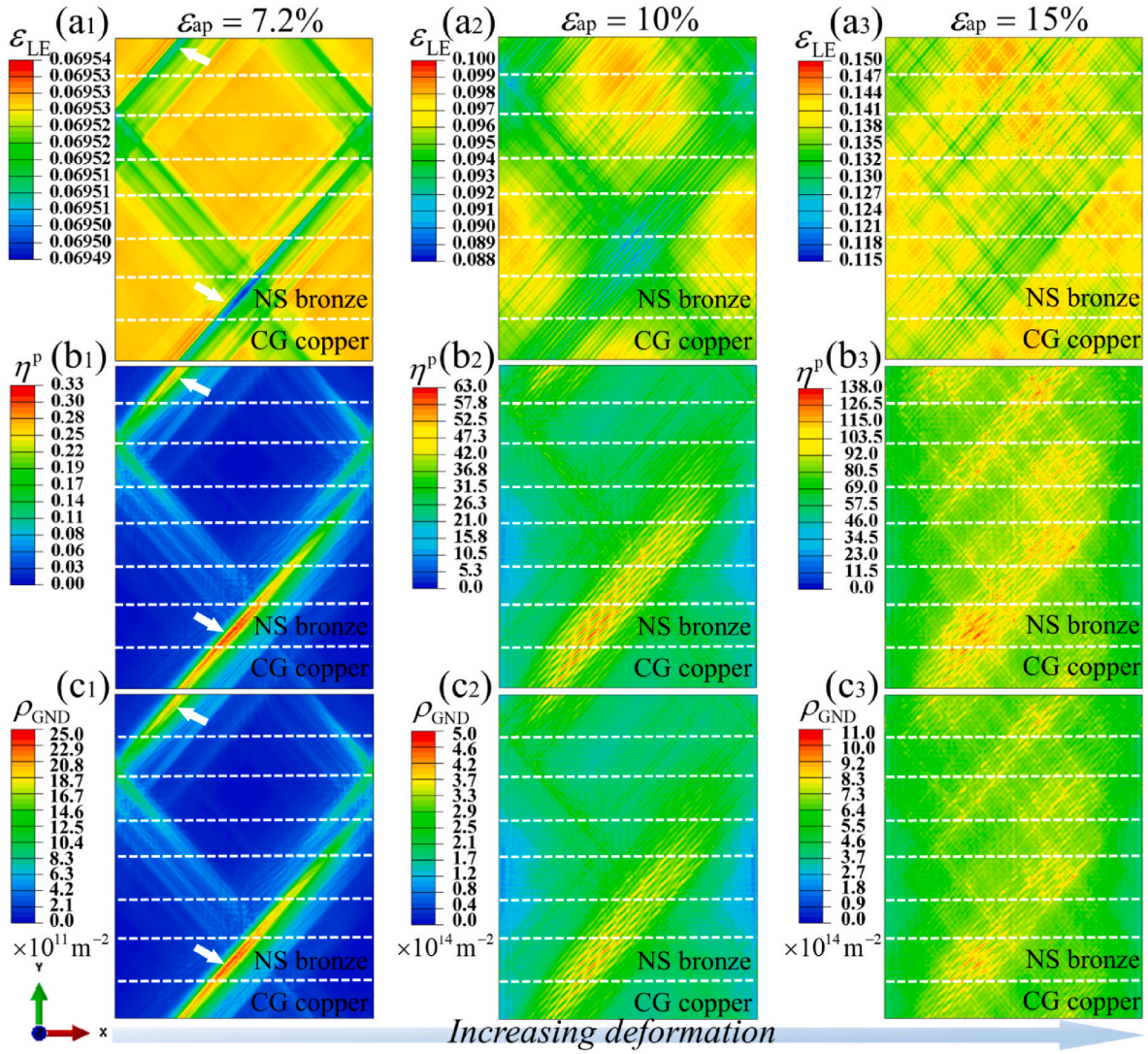

Fig. 7. Simulated contours of Laminate 3.7 at applied engineering strains of 7.2 %, 10 %, and 15 %: (a) Logarithmic strain (LE); (b) Effective plastic strain gradient; (c) GND density. The white dotted lines represent the layer interfaces. The distribution of GNDs is similar to that of the plastic strain gradient at different strains. A high strain gradient indicates high strain heterogeneity in localized regions, as marked by the white arrows.

Due to its limited strain hardening capacity, the NS bronze layer preferentially experiences plastic instability and strain localization during deformation. This non-uniform deformation gives rise to a strain gradient accompanied by generating numerous GNDs. Consequently, the accumulation of GNDs enhances the strain hardening ability of the NS bronze layer, effectively suppressing excessive strain localization and forming several dispersed strain bands in the surrounding region. As deformation progresses, these individual strain bands grow, triggering

further strain gradient and GND generation, thereby promoting enhanced strain hardening over a wider area. This self-feedback process between the strain gradient and strain bands persists during deformation, as illustrated in Fig. 8, ultimately resulting in dense and dispersed strain bands. Notably, the plastic strain gradient effect becomes significant when the layer thickness drops below a few micrometers. As a result, HS laminates with thicker layers generally do not exhibit dispersed strain bands comparable to those observed in Laminate-3.7 and Laminate-7.5.

The above analysis demonstrates the pivotal role of the strain gradient effect in strain banding. The inherent structural heterogeneity of HS laminates results in the strain partition and strain gradient, the plastic strain gradient effect in turn facilitates the formation of strain bands. These strain bands effectively sustain stable strain delocalization and promote the generation of GNDs, thereby enhancing strain hardening and contributing to the strength-ductility synergy. The simulation results in this study advance our understanding of the mechanisms governing strain banding in HS laminates.

3.5. Effect of heterogeneous deformation

The impact of heterogeneous deformation (strain partition and strain banding) on the mechanical behavior of HS laminates can be further elucidated through the analysis of simulation results. Fig. 9(a) gives the evolution of strain distribution along a path traversing three layers, as marked by the black dotted arrow in Fig. 5(b_1). Initially, at an applied strain of 7 %, all regions along this path undergo the same deformation. However, as deformation progresses, a gradual development of inhomogeneous strain distribution can be observed, owing to the formation of strain bands, as evident in Fig. 7(a_2). As deformation continues, the strain disparity between different regions within the path intensifies, leading to an enhanced degree of deformation inhomogeneity. Importantly, severe localized strain is not observed. This phenomenon can be attributed to the presence of dispersed strain bands, which effectively impede strain localization and early fracture, enabling all regions to sustain deformation throughout the loading process. This mechanism ensures the optimal utilization of material properties and contributes to the uniform elongation, promoting a favorable combination of strength and ductility.

Heterogeneous deformation also gives rise to an extra strain hardening phenomenon known as HDI hardening [2]. Fig. 9(b) displays the strain hardening curves derived from the true strain-stress curves depicted in Fig. 3(b). Remarkably, both Laminate-3.7 and Laminate-7.5 exhibit significant extra strain hardening, with Laminate-3.7 demonstrating earlier and more obvious hardening. From Eq. (2), the increase in flow stress can be attributed to the improvement in both SSD and GND densities. Moreover, Fig. 3(c) reveals a notable correspondence between the onset of GND accumulation and the initiation of extra strain hardening in Fig. 9(b), suggesting a direct association between the two phenomena. In HS laminates, GNDs accommodate the inhomogeneous deformation, consequently reinforcing the link between HDI hardening and the strain gradient effect [36]. Additionally, the thickness of layers also influences HDI hardening. Fig. 9(b) demonstrates that HS laminates with a layer thickness exceeding 15 μm exhibit negligible extra hardening due to the weakened plastic strain gradient effect and low GND density, as confirmed in Fig. 3(c).

Based on the above discussion, it is evident that heterogeneous deformation has a significant synergistic effect on the strain hardening and uniform elongation of HS laminates. The strain delocalization is achieved through the formation of dispersed stable strain bands and the generation of GNDs, thereby facilitating strain hardening. These mechanisms are inherently underpinned by the strain gradient effect. However, it is important to note that the simulations conducted in this study did not capture the interface affected zone (IAZ) characterized by an evident strain gradient [14]. Consequently, the influence of IAZ width on the mechanical properties of HS laminates could not be fully addressed. The authors anticipate that a nonlocal crystal plasticity model considering the microstructure heterogeneity would better capture slip mismatch near the layer interface. In the future, the authors intend to employ crystal plasticity simulations to provide insights into the intrinsic relationship between interfacial strain gradient and GNDs.

4. Conclusions

This study employed the CMSG plasticity model in conjunction with finite element analysis to investigate the deformation mechanism of HS laminates comprising NS bronze and CG copper layers. The primary focus of this investigation was to elucidate the role of stress/strain partition in the layer interactions and the overall mechanical behavior. The evolutions of stress, strain, strain gradient, and GND density in each layer were carefully analyzed. The key findings are summarized as follows:

(1) The dissimilar mechanical properties of the CG copper and NS bronze layers give rise to stress partition during deformation, resulting in a continuous evolution of the stress distribution among the layers. As significant plastic deformation occurs, there is an increase in the stress percent of the CG copper layer, accompanied by a reduction in that of the NS bronze layer. This phenomenon indicates the stress transfer from the hard zone to the soft zone. Moreover, the stress difference between the layers decreases as the layer thickness reduces.

(2) In addition to stress partition, strain partition is observed in HS laminates. Notably, dense dispersed strain bands are formed in the laminates with a relatively thinner layer thickness, which is consistent with the experimental measurement using micro-DIC. The formation of these strain bands is closely associated with the

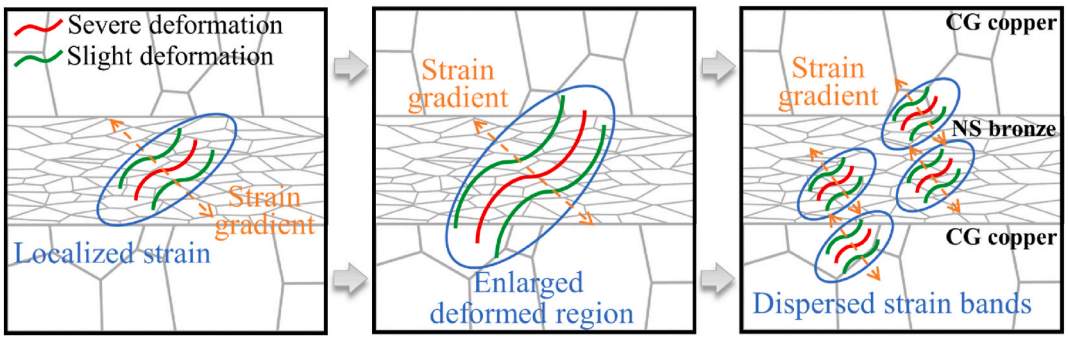

Fig. 8. Schematic diagram of the formation of dispersed strain bands in HS laminates: localized deformation first occurs in the NS bronze layer due to the poor strain hardening capacity. With increasing applied strain, the region with localized strain is enlarged, accompanied by a remarkable strain gradient. The GNDs induced by strain gradient make the NS bronze layer harden. Thus, the strain localization no longer expands and turns to form several dispersed strain bands.

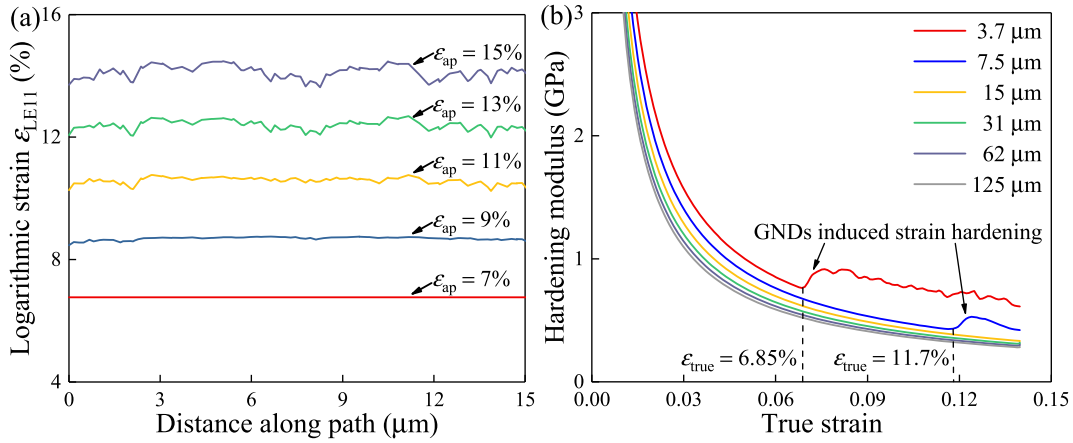

Fig. 9. Effects of heterogeneous deformation on the mechanical behavior of HS laminates: (a) strain distributions along the path defined in Fig. 5(b_1) at different applied engineering strains, non-uniform deformation occurs, but no severe strain localization appears; (b) Strain hardening curves of HS laminates with different layer thicknesses, GNDs caused by heterogeneous deformation result in obvious extra strain hardening in HS laminates with thinner layers.

plastic strain gradient, which effectively prevents the occurrence of severe strain localization.

(3) Heterogeneous deformation is identified as the key driver behind improving the uniform elongation of HS laminates. On the one hand, dispersed strain bands allow a large region to accommodate deformation, thereby preventing plastic instability. On the other hand, the generation of GNDs resulting from plastic strain gradients contributes to extra strain hardening.

This study significantly enhances our understanding of the deformation mechanisms in HS laminates, including stress/strain partition and strain banding. Furthermore, the finite element simulation methodology employed herein holds promise as a valuable tool for the design and optimization of laminated materials to achieve superior mechanical performance.

Declaration of competing interest

The authors declare that they have no known competing financial interests or personal relationships that could have appeared to influence the work reported in this paper.

Data availability

Data will be made available on request.

Acknowledgements

This work was supported by the National Natural Science Foundation of China (92263201, 51931003, 12202423, 12302280), the Fundamental Research Funds for the Central Universities (2022SCU12094), the Project funded by China Postdoctoral Science Foundation (2022M722253), the Sichuan University Postdoctoral Interdisciplinary Innovation Fund (JCXK2238).

Appendix A. Computation of the plastic strain gradient

The plastic strain components were stored at each integration point using modules in the UMAT. The increment of the effective strain gradient under rate-proportional loading conditions can be expressed by [74].

$$\Delta\eta^{p} = \sqrt{\frac{1}{4}\Delta\eta^{p}_{ijk}\Delta\eta^{p}_{ijk}}, \tag{A1}$$

where $\Delta\eta^{p}_{ijk}$ is calculated based on the MSG plasticity theory [60]

$$\Delta\eta^{p}_{ijk} = \Delta\varepsilon^{p}_{ik,j} + \Delta\varepsilon^{p}_{jk,i} - \Delta\varepsilon^{p}_{ij,k}. \tag{A2}$$

The plastic strain increment is interpolated in the iso-parametric space using its value at the integration points. The plastic strain gradient increment is then obtained through the differentiation of the shape function. Consequently, the effective plastic strain gradient η^{p} at the element level is calculated. As an illustration, the interpolation and calculation processes for an 8-node quadrilateral quadratic plane strain element are depicted inFig. A1.

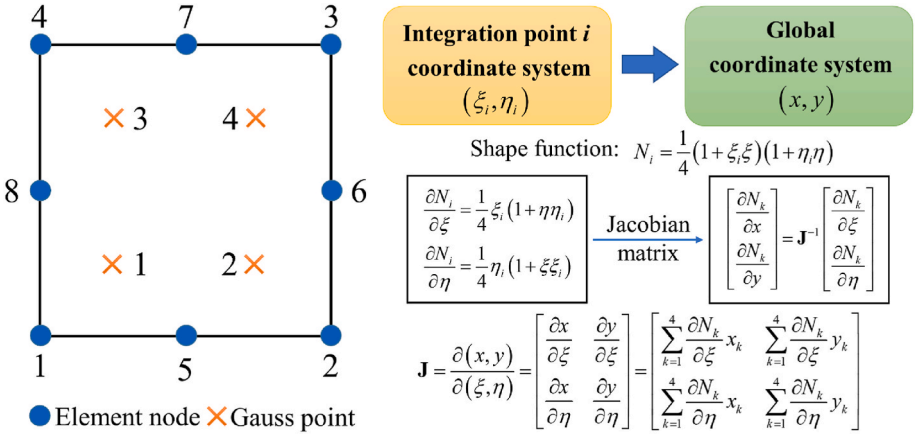

Fig. A1. Schematic diagram of nodes and Gauss integration point in the quadrilateral quadratic plane strain elements, the process of computing effective plastic strain gradient is also shown.

References

[1] Y. Zhu, X. Wu, Heterostructured materials, Prog. Mater. Sci. 131 (2023), 101019.
[2] X.T. Fang, G.Z. He, C. Zheng, X.L. Ma, D. Kaoumi, Y.S. Li, Y.T. Zhu, Effect of heterostructure and hetero-deformation induced hardening on the strength and ductility of brass, Acta Mater. 186 (2020) 644–655.
[3] P. Sathiyamoorthi, H.S. Kim, High-entropy alloys with heterogeneous microstructure: processing and mechanical properties, Prog. Mater. Sci. 123 (2022), 100709.
[4] T.H. Fang, W.L. Li, N.R. Tao, K. Lu, Revealing extraordinary intrinsic tensile plasticity in gradient nano-grained copper, Science 331 (2011) 1587.
[5] X. Lu, Y. Gui, Z. Fu, N. Ao, S. Wu, X. Zhang, Mechanical behavior and microstructure-property correlation of a metastable interstitial high entropy alloy with hierarchical gradient structures, Mater. Char. 204 (2023), 113232.
[6] K.A. Andrianova, I.N. Sidorov, L.M. Amirova, Modeling and study of properties distribution in graded polymer materials, Results Eng. 19 (2023), 101299.
[7] Y. Ma, H. Chen, M.-X. Zhang, A. Addad, Y. Kong, M.B. Lezaack, W. Gan, Z. Chen, G. Ji, Break through the strength-ductility trade-off dilemma in aluminum matrix composites via precipitation-assisted interface tailoring, Acta Mater. 242 (2023), 118470.
[8] S. Liu, D. Xia, H. Yang, G. Huang, F. Yang, X. Chen, A. Tang, B. Jiang, F. Pan, Mechanical properties and deformation mechanism in Mg-Gd alloy laminate with dual-heterostructure grain size and texture, Int. J. Plast. 157 (2022), 103371.
[9] Y. Zhu, K. Ameyama, P.M. Anderson, I.J. Beyerlein, H. Gao, H.S. Kim, E. Lavernia, S. Mathaudhu, H. Mughrabi, R.O. Ritchie, N. Tsuji, X. Zhang, X. Wu, Heterostructured materials: superior properties from hetero-zone interaction, Mater. Res. Lett. 9 (2021) 1–31.
[10] X. Wu, Y. Zhu, Gradient and lamellar heterostructures for superior mechanical properties, MRS Bull. 46 (2021) 244–249.
[11] K. Wu, Y. Song, X. Zhang, S. Zhang, Z. Zheng, X. Gong, L. He, H.-B. Yao, Y. Ni, A prestressing strategy enabled synergistic energy-dissipation in impact-resistant nacre-like structures, Adv. Sci. 9 (2022), 2104867.
[12] W. Chen, W. He, Z. Chen, B. Jiang, Q. Liu, Extraordinary room temperature tensile ductility of laminated Ti/Al composite: roles of anisotropy and strain rate sensitivity, Int. J. Plast. 133 (2020), 102806.
[13] S. Guan, D. Wan, K. Solberg, F. Berto, T. Welo, T.M. Yue, K.C. Chan, Additively manufactured CrMnFeCoNi/AlCoCrFeNiTi0.5 laminated high-entropy alloy with enhanced strength-plasticity synergy, Scripta Mater. 183 (2020) 133–138.
[14] C.X. Huang, Y.F. Wang, X.L. Ma, S. Yin, H.W. Höppel, M. Göken, X.L. Wu, H.J. Gao, Y.T. Zhu, Interface affected zone for optimal strength and ductility in heterogeneous laminate, Mater. Today 21 (2018) 713–719.
[15] S. Jiang, R. Lin Peng, X. Zhao, L. Zuo, N. Jia, Deformation incompatibility enables hetero-deformation induced strengthening in Ti/Nb laminates, Mater. Res. Lett. 11 (2023) 126–133.
[16] B.X. Liu, L.J. Huang, B. Wang, L. Geng, Effect of pure Ti thickness on the tensile behavior of laminated Ti–TiBw/Ti composites, Mater. Sci. Eng. A 617 (2014) 115–120.
[17] Y. Xia, H. Wu, K. Miao, X. Li, C. Xu, L. Geng, H. Xie, G. Fan, Effects of the layer thickness ratio on the enhanced ductility of laminated aluminum, J. Mater. Sci. Technol. 111 (2022) 256–267.
[18] D. Li, G. Fan, X. Huang, D. Juul Jensen, K. Miao, C. Xu, L. Geng, Y. Zhang, T. Yu, Enhanced strength in pure Ti via design of alternating coarse- and fine-grain layers, Acta Mater. 206 (2021), 116627.
[19] I. Hasanuddin, I. Mawardi, N. Nurdin, R.P. Jaya, Evaluation of properties of hybrid laminated composites with different fiber layers based on Coir/Al2O3 reinforced composites for structural application, Results Eng. 17 (2023), 100948.
[20] R. Kocich, A. Macháčková, F. Fojtík, Comparison of strain and stress conditions in conventional and ARB rolling processes, Int. J. Mech. Sci. 64 (2012) 54–61.
[21] V. Yousefi Mehr, M.R. Toroghinejad, On the texture evolution of aluminum-based composites manufactured by ARB process: a review, J. Mater. Res. Technol. 21 (2022) 1095–1109.
[22] Y. Chen, J. Nie, F. Wang, H. Yang, C. Wu, X. Liu, Y. Zhao, Revealing hetero-deformation induced (HDI) stress strengthening effect in laminated Al-(TiB2+TiC) p/6063 composites prepared by accumulative roll bonding, J. Alloys Compd. 815 (2020), 152285.
[23] S. Jiang, R.L. Peng, Z. Hegedűs, T. Gnäupel-Herold, J.J. Moverare, U. Lienert, F. Fang, X. Zhao, L. Zuo, N. Jia, Micromechanical behavior of multilayered Ti/Nb composites processed by accumulative roll bonding: an in-situ synchrotron X-ray diffraction investigation, Acta Mater. 205 (2021), 116546.
[24] Y. Du, G. Fan, T. Yu, N. Hansen, L. Geng, X. Huang, Laminated Ti-Al composites: processing, structure and strength, Mater. Sci. Eng. A 673 (2016) 572–580.
[25] M.Y. Khalid, R. Umer, K.A. Khan, Review of recent trends and developments in aluminium 7075 alloy and its metal matrix composites (MMCs) for aircraft applications, Results Eng. 20 (2023), 101372.
[26] T. Liu, B. Song, G. Huang, X. Jiang, S. Guo, K. Zheng, F. Pan, Preparation, structure and properties of Mg/Al laminated metal composites fabricated by roll-bonding, a review, J. Magnesium Alloys 10 (2022) 2062–2093.
[27] Z. Zhou, J. Li, Q. Mao, Y. Yue, S. Wang, Y. Li, Heterostructured copper-brass laminates with gradient transition layer, J. Mater. Res. Technol. 23 (2023) 5534–5546.
[28] N. Madkhali, C. Prasad, K. Malkappa, H.Y. Choi, V. Govinda, I. Bahadur, R. A. Abumousa, Recent update on photocatalytic degradation of pollutants in waste water using TiO2-based heterostructured materials, Results Eng. 17 (2023), 100920.
[29] T.C. Herring, T. Nyomboi, J.N. Thuo, Ductility and cracking behavior of reinforced coconut shell concrete beams incorporated with coconut shell ash, Results Eng. 14 (2022), 100401.
[30] J.C. Stotts, G.B. Thompson, C.R. Weinberger, Modeling the diffusion-controlled phase transformations in transition metal carbide multilayer composites, Results Eng. 18 (2023), 101106.
[31] J.G. Kim, M.J. Jang, H.K. Park, K.-G. Chin, S. Lee, H.S. Kim, Back-stress effect on the mechanical strength of TWIP-IF steels layered sheet, Met. Mater. Int. 25 (2019) 912–917.
[32] C.C. Tasan, M. Diehl, D. Yan, C. Zambaldi, P. Shanthraj, F. Roters, D. Raabe, Integrated experimental–simulation analysis of stress and strain partitioning in multiphase alloys, Acta Mater. 81 (2014) 386–400.
[33] E. Ma, T. Zhu, Towards strength–ductility synergy through the design of heterogeneous nanostructures in metals, Mater. Today 20 (2017) 323–331.
[34] H. Zhou, C. Huang, X. Sha, L. Xiao, X. Ma, H.W. Höppel, M. Göken, X. Wu, K. Ameyama, X. Han, Y. Zhu, In-situ observation of dislocation dynamics near heterostructured interfaces, Mater. Res. Lett. 7 (2019) 376–382.
[35] H. Mughrabi, Dual role of deformation-induced geometrically necessary dislocations with respect to lattice plane misorientations and/or long-range internal stresses, Acta Mater. 54 (2006) 3417–3427.
[36] Y. Zhu, X. Wu, Perspective on hetero-deformation induced (HDI) hardening and back stress, Mater. Res. Lett. 7 (2019) 393–398.
[37] X. Wu, Y. Zhu, Heterogeneous materials: a new class of materials with unprecedented mechanical properties, Mater. Res. Lett. 5 (2017) 527–532.
[38] F. Liang, B. Zhang, Y. Yong, X.-M. Luo, G.-P. Zhang, Enhanced strain delocalization through formation of dispersive micro shear bands in laminated Ni, Int. J. Plast. 132 (2020), 102745.
[39] Y. Wang, Y. Wei, Z. Zhao, H. Long, Z. Lin, F. Guo, Q. He, C. Huang, Y. Zhu, Activating dispersed strain bands in tensioned nanostructure layer for high ductility: the effects of microstructure inhomogeneity, Int. J. Plast. 149 (2022), 103159.

[40] J. Zhao, B. Liu, Y. Wang, Y. Liang, J. Li, X. Zhang, Dispersed strain bands promote the ductility of gradient nano-grained material: a strain gradient constitutive modeling considering damage effect, Mech. Mater. 179 (2023), 104599.
[41] Z.-L. Tian, Y.-J. Wang, Y. Chen, L.-H. Dai, Strain gradient drives shear banding in metallic glasses, Phys. Rev. B 96 (2017), 094103.
[42] Y. Xia, H. Fang, X. Bai, X. Li, J. Wang, H. Wu, L. Geng, G. Fan, Revealing the interface-mediated dislocation behavior and its role in delocalizing strain band in laminated aluminum, Mater. Sci. Eng. A 887 (2023), 145736.
[43] X. Lu, X. Zhang, M. Shi, F. Roters, G. Kang, D. Raabe, Dislocation mechanism based size-dependent crystal plasticity modeling and simulation of gradient nano-grained copper, Int. J. Plast. 113 (2019) 52–73.
[44] X. Lu, J. Zhao, Z. Wang, B. Gan, J. Zhao, G. Kang, X. Zhang, Crystal plasticity finite element analysis of gradient nanostructured TWIP steel, Int. J. Plast. 130 (2020), 102703.
[45] L. Zhu, S. Qu, X. Guo, J. Lu, Analysis of the twin spacing and grain size effects on mechanical properties in hierarchically nanotwinned face-centered cubic metals based on a mechanism-based plasticity model, J. Mech. Phys. Solid. 76 (2015) 162–179.
[46] L. Zhu, H. Ruan, A. Chen, X. Guo, J. Lu, Microstructures-based constitutive analysis for mechanical properties of gradient-nanostructured 304 stainless steels, Acta Mater. 128 (2017) 375–390.
[47] J. Li, S. Chen, X. Wu, A.K. Soh, A physical model revealing strong strain hardening in nano-grained metals induced by grain size gradient structure, Mater. Sci. Eng. A 620 (2015) 16–21.
[48] J. Li, A.K. Soh, Modeling of the plastic deformation of nanostructured materials with grain size gradient, Int. J. Plast. 39 (2012) 88–102.
[49] L. Zhu, J. Lu, Modelling the plastic deformation of nanostructured metals with bimodal grain size distribution, Int. J. Plast. 30–31 (2012) 166–184.
[50] J. Li, T. Chen, T. Chen, Z. Yun, X. Xia, Computational modelling of frictional deformation of bimodal nanograined metals, Int. J. Mech. Sci. 222 (2022), 107220.
[51] J. Li, Q. Zhang, R. Huang, X. Li, H. Gao, Towards understanding the structure–property relationships of heterogeneous-structured materials, Scripta Mater. 186 (2020) 304–311.
[52] S.K. Georgantzinos, P.A. Antoniou, C. Spitas, A multi-scale computational framework for the hygro-thermo-mechanical analysis of laminated composite structures with carbon nanotube inclusions, Results Eng. 17 (2023), 100904.
[53] A. Mirzakhani, A. Assempour, The effects of microstructural parameters on the tension-compression mechanical behavior of extruded Mg-XY rods using crystal plasticity finite element modeling, Results Eng. 17 (2023), 100834.
[54] H.F. Isleem, N.D.K.R. Chukka, A. Bahrami, S. Oyebisi, R. Kumar, T. Qiong, Nonlinear finite element and analytical modelling of reinforced concrete filled steel tube columns under axial compression loading, Results Eng. 19 (2023), 101341.
[55] Y. Zhang, Z. Cheng, L. Lu, T. Zhu, Strain gradient plasticity in gradient structured metals, J. Mech. Phys. Solid. 140 (2020), 103946.
[56] H. Lyu, M. Hamid, A. Ruimi, H.M. Zbib, Stress/strain gradient plasticity model for size effects in heterogeneous nano-microstructures, Int. J. Plast. 97 (2017) 46–63.
[57] J. Zhao, X. Lu, J. Liu, C. Bao, G. Kang, M. Zaiser, X. Zhang, The tension-compression behavior of gradient structured materials: a deformation-mechanism-based strain gradient plasticity model, Mech. Mater. 159 (2021), 103912.
[58] Y. Wang, Y. Zhu, Z. Yu, J. Zhao, Y. Wei, Hetero-zone boundary affected region: a primary microstructural factor controlling extra work hardening in heterostructure, Acta Mater. 241 (2022), 118395.
[59] J. Li, S. Chen, G.J. Weng, W. Lu, A micromechanical model for heterogeneous nanograined metals with shape effect of inclusions and geometrically necessary dislocation pileups at the domain boundary, Int. J. Plast. 144 (2021), 103024.
[60] H. Gao, Y. Huang, W.D. Nix, J.W. Hutchinson, Mechanism-based strain gradient plasticity— I, Theor. J. Mech. Phys. Solid. 47 (1999) 1239–1263.
[61] Y. Huang, H. Gao, W.D. Nix, J.W. Hutchinson, Mechanism-based strain gradient plasticity—II. Analysis, J. Mech. Phys. Solid. 48 (2000) 99–128.
[62] N.A. Fleck, J.W. Hutchinson, A phenomenological theory for strain gradient effects in plasticity, J. Mech. Phys. Solid. 41 (1993) 1825–1857.
[63] S. Wulfinghoff, S. Forest, T. Böhlke, Strain gradient plasticity modeling of the cyclic behavior of laminate microstructures, J. Mech. Phys. Solid. 79 (2015) 1–20.
[64] N.A. Fleck, J.R. Willis, A mathematical basis for strain-gradient plasticity theory. Part II: tensorial plastic multiplier, J. Mech. Phys. Solid. 57 (2009) 1045–1057.
[65] K.E. Aifantis, J.R. Willis, The role of interfaces in enhancing the yield strength of composites and polycrystals, J. Mech. Phys. Solid. 53 (2005) 1047–1070.
[66] A. Panteghini, L. Bardella, On the role of higher-order conditions in distortion gradient plasticity, J. Mech. Phys. Solid. 118 (2018) 293–321.
[67] Y. Huang, S. Qu, K.C. Hwang, M. Li, H. Gao, A conventional theory of mechanism-based strain gradient plasticity, Int. J. Plast. 20 (2004) 753–782.
[68] J. Wang, C. Yang, P.D. Hodgson, Strain gradients in Cu–Fe thin films and multilayers during micropillar compression, Mater. Sci. Eng. A 651 (2016) 146–154.
[69] R. Yuan, H. Du, Modeling the effects of interface spacing on the mechanical properties of heterogeneous laminates, Comput. Mater. Sci. 173 (2020), 109391.
[70] J. Zhao, M. Zaiser, X. Lu, B. Zhang, C. Huang, G. Kang, X. Zhang, Size-dependent plasticity of hetero-structured laminates: a constitutive model considering deformation heterogeneities, Int. J. Plast. 145 (2021), 103063.
[71] G.I. Taylor, The mechanism of plastic deformation of crystals. Part I.-Theoretical, Proc. R. Soc. London, A 145 (1934) 362–387.
[72] J.F. Nye, Some geometrical relations in dislocated crystals, Acta Metall. 1 (1953) 153–162.
[73] M.F. Ashby, The deformation of plastically non-homogeneous materials, Philos. Mag. A 21 (1970) 399–424.
[74] E. Martínez-Pañeda, C. Betegón, Modeling damage and fracture within strain-gradient plasticity, Int. J. Solid Struct. 59 (2015) 208–215.
[75] A. Misra, J.P. Hirth, R.G. Hoagland, Length-scale-dependent deformation mechanisms in incoherent metallic multilayered composites, Acta Mater. 53 (2005) 4817–4824.
[76] S.L. Omairey, P.D. Dunning, S. Sriramula, Development of an ABAQUS plugin tool for periodic RVE homogenisation, Eng. Comput. 35 (2019) 567–577.
[77] R.K. Nutor, Q. Cao, R. Wei, Q. Su, G. Du, X. Wang, F. Li, D. Zhang, J.-Z. Jiang, A dual-phase alloy with ultrahigh strength-ductility synergy over a wide temperature range, Sci. Adv. 7 (2021), eabi4404.
[78] M. Zhou, Y. Geng, Y. Zhang, Y. Ban, X. Li, Y. Jia, S. Liang, B. Tian, Y. Liu, A. A. Volinsky, Enhanced mechanical properties and high electrical conductivity of copper alloy via dual-nanoprecipitation, Mater. Char. 195 (2023), 112494.
[79] J.V. Gordon, R.E. Lim, M.J. Wilkin, D.C. Pagan, R.A. Lebensohn, A.D. Rollett, Evaluating the grain-scale deformation behavior of a single-phase FCC high entropy alloy using synchrotron high energy diffraction microscopy, Acta Mater. 215 (2021), 117120.
[80] O.M. Injor, O.O. Daramola, B.O. Adewuyi, A.A. Adediran, M.M. Ramakokovhu, R. E. Sadiku, E.T. Akinlabi, Grain refinement of Al–Zn–Mg alloy during equal channel angular pressing (ECAP), Results Eng. 16 (2022), 100739.
[81] J. Choung, S.-R. Cho, Study on true stress correction from tensile tests, J. Mater. Res. Technol. 22 (2008) 1039–1051.
[82] Y.F. Wang, C.X. Huang, Q. He, F.J. Guo, M.S. Wang, L.Y. Song, Y.T. Zhu, Heterostructure induced dispersive shear bands in heterostructured Cu, Scripta Mater. 170 (2019) 76–80.
[83] Q. Cheng, Y. Wang, W. Wei, F. Guo, Q. He, M. Wang, C. Huang, Superior strength-ductility synergy achieved by synergistic strengthening and strain delocalization in a gradient-structured high-manganese steel, Mater. Sci. Eng. A 825 (2021), 141853.
[84] X. Wu, M. Yang, F. Yuan, G. Wu, Y. Wei, X. Huang, Y. Zhu, Heterogeneous lamella structure unites ultrafine-grain strength with coarse-grain ductility, Proc. Natl. Acad. Sci. USA 112 (2015) 14501–14505.